Crystalline/amorphous Ni/Ni$_x$S$_y$ supported on hierarchical porous nickel foam for high-current-density hydrogen evolution

Bo Zhong [a], Sijie Wan [a], Panyong Kuang [b], Bei Cheng [a], Luo Yu [b,*], Jiaguo Yu [a,b,**]

[a] State Key Laboratory of Advanced Technology for Materials Synthesis and Processing, Wuhan University of Technology, Wuhan 430070, PR China
[b] Laboratory of Solar Fuel, Faculty of Materials Science and Chemistry, China University of Geosciences, 68 Jincheng Street, Wuhan 430078, PR China

ARTICLE INFO

ABSTRACT

Manufacturing efficient and durable electrodes for alkaline water electrolysis under high-current-density conditions is a great challenge. Herein, Ni/Ni$_x$S$_y$ heterostructure was grown on designed porous nickel foam (PNF) to construct Ni/Ni$_x$S$_y$-PNF electrode by a facile and scalable method for alkaline hydrogen evolution reaction (HER). The hierarchical porous structure and super-hydrophilic surface of Ni/Ni$_x$S$_y$-PNF accelerate the mass transfer and bubble detachment at high current densities. Theoretical calculations reveals that the enhanced HER activity of Ni/Ni$_x$S$_y$ heterostructure is attributed to the stronger H$_2$O adsorption. The resulting Ni/Ni$_x$S$_y$-PNF electrode achieves current densities of 100 and 500 mA cm^{-2} at low overpotentials of 61 and 121 mV, respectively. When applied for overall water splitting, the Ni/Ni$_x$S$_y$-PNF||Fe-Ni$_3$S$_2$-PNF electrolyser reaches a current density of 10 mA cm^{-2} at an extremely low voltage of 1.32 V. This work provides an effective strategy for fabricating high-performance electrodes for practical water electrolysis.

1. Introduction

Green hydrogen, produced by water electrolysis, is a promising sustainable energy carrier and a desirable alternative to fossil fuels [1–12]. However, the lack of efficient and durable electrodes for the hydrogen evolution reaction (HER) limits the efficiency of water electrolysis technology, especially in alkaline media [13–18]. Although the state-of-art Pt-based electrocatalysts are highly active, they suffer from high cost and unsatisfied stability at high current densities [19–22]. Besides, efficient mass transfer and mechanical stability of the electrodes are extremely important for practical applications under industrial conditions [23–25]. Thus, developing active and durable electrodes is urgent yet challenging for large-scale alkaline water electrolysis.

The HER kinetics in alkaline electrolytes is 2–3 orders of magnitude slower than that in acidic media, which results from the additional water dissociation step [26–29]. Although numerous strategies, such as heteroatom doping, morphology tuning, and defect regulation, have been investigated to improve alkaline HER performance, heterostructure engineering has attracted particular attention due to its inherent anisotropy and high flexibility [30–33]. For example, Pt$_3$Ni/NiS heterostructure with tunable interfaces exhibits increased HER performance, where the NiS promotes water dissociation and Pt$_3$Ni effectively convents protons to hydrogen [34]. The electron transfer at the interface of NiS/NiS$_2$/Ni$_3$S$_4$ heterostructure leads to electron accumulation on NiS and hole accumulation on Ni$_3$S$_4$/NiS$_2$, which balances the active hydrogen and H$_2$O adsorption and enhances the HER activity [35]. NiMoO$_x$/NiMoS heterostructure array with optimized adsorption energy and accelerated water splitting kinetic also displays excellent activity and durability for HER [30]. The heterostructures are generally fabricated by complex high-temperature methods, therefore, it is a challenge to find a facile and scalable one-step synthesis method at room temperature [35–37]. Nevertheless, the stability of currently reported electrocatalysts is still difficult to meet the industrial applications requirements.

On the other hand, electrodes for practical alkaline water electrolysis are required to function in harsh conditions, *e.g.*, high current densities, long working periods, and high temperatures [38]. Conventional powder catalysts coated on substrates suffer from low electrical conductivity, poor mechanical stability, and inefficient mass transfer, which significantly decrease the HER efficiency [39]. Self-supported electrodes

* Corresponding author.
** Corresponding author at: State Key Laboratory of Advanced Technology for Materials Synthesis and Processing, Wuhan University of Technology, Wuhan 430070, PR China

E-mail addresses: luoyu@cug.edu.cn (L. Yu), yujiaguo93@cug.edu.cn (J. Yu).

with intimate contact between catalysts and substrates improve conductivity and mechanical stability [40,41]. In addition, the hierarchical porous structure can accelerate the external mass transfer of reactant consumption and product accumulation at high current densities [42,43]. For instance, the Chevrel phase $CuMo_6S_8$/Cu electrode with strong binding and weak bubble adhesion at the interface achieves fast charge transfer kinetics and high HER activity at high current densities [38]. The super-hydrophilic $Ru/(Fe, Ni)(OH)_2$ electrode exhibits rapid gas release, efficient electron transportation, and mass transfer, which contribute to excellent activity and stability at high current densities [44]. Therefore, it is promising to construct advanced self-standing electrodes with highly active catalysts and hierarchical porous structures for practical alkaline water electrolysis.

Here we coupled porous nickel foam (PNF) substrate with Ni/Ni_xS_y heterostructure to construct an efficient and durable self-standing Ni/Ni_xS_y-PNF electrode for alkaline HER. The Ni/Ni_xS_y-PNF electrode was fabricated *via* a two-step electrodeposition process. The PNF substrate prepared by a bubble template method had porous structure and superhydrophilic surface, which provided more active sites for catalysts loading and facilitated mass transfer and bubble detachment at high-current-density conditions. Notably, the Ni/Ni_xS_y heterostructure was subsequently grown on the PNF substrate by a facile and scalable *in-situ* co-electrodeposition process. The resulting hierarchical Ni/Ni_xS_y-PNF electrode with a highly active Ni/Ni_xS_y heterostructure interface and hierarchical porous structure possessed remarkable HER activity and impressive stability at high current densities. It exhibited a low overpotential of 61 mV to reach 100 mA cm^{-2} and a low Tafel slope of 83 mV dec^{-1} in 1.0 M KOH. Operando electrochemical impedance spectroscopy (EIS) tests indicated that the Ni/Ni_xS_y heterostructure interface facilitated the sluggish water dissociation step, leading to a faster HER kinetic process. When coupled with a $Fe-Ni_3S_2$-PNF electrode in a two-electrode water splitting system, the Ni/Ni_xS_y-PNF||$Fe-Ni_3S_2$-PNF electrolyser only required a voltage of 1.32 V to reach 10 mA cm^{-2}. Notably, it also performed stable alkaline water electrolysis at 500 mA cm^{-2} for over 120 h under industrial conditions (30 wt% KOH, 85 °C). This facile and scalable method can be extended to fabricate advanced electrodes for practical alkaline water electrolysis.

2. Experimental section

2.1. Chemicals

All chemicals were of analytical grade and used directly as received without further purification. Deionized water was used in all experiments. Hydrochloric acid (HCl), ethanol (C_2H_6O), nickel (II) chloride hexahydrate ($NiCl_2 \cdot 6 H_2O$), ammonium chloride (NH_4Cl), thiourea (CH_4N_2S), and potassium hydroxide (KOH) were purchased from Sinopharm Chemical Reagent Co. Ltd.

2.2. Synthesis of Ni/Ni_xS_y-PNF electrode

We used a two-step electrodeposition method to fabricate Ni/Ni_xS_y-PNF electrode. Commercial Ni foam (NF) was treated with 1.0 M HCl, ethanol, and deionized water under sonication for 30 min to remove the surface nickel oxide layer and impurities. Firstly, the PNF was constructed in a standard two-electrode system at room temperature, using NF and graphite rod as the working electrode and counter electrode, respectively. The electrolyte consisted of 0.1 M $NiCl_2$ and 2.0 M NH_4Cl. The dynamic bubble template method was performed at a cathodic current density of 1.0 A cm^{-2} for 600 s. Then the PNF was rinsed with deionized water several times and dried in air. Afterward, another electrodeposition process was carried out in a three-electrode system at room temperature, in which the prepared PNF, graphite rod, and Ag/AgCl electrode were employed as working electrode, counter electrode, and reference electrode, respectively. Then 1.19 g $NiCl_2$, 3.8 g CH_4N_2S, and 300 mg NH_4Cl were dissolved in 50 mL deionized water to form the

electrolyte. The electrodeposition was carried out at a constant potential of -1.8 V (*vs.* Ag/AgCl) for 600 s. The as-prepared electrode was then rinsed with deionized water, dried in air, and directly used for electrochemical tests. The Ni-PNF and NiS-PNF electrodes were fabricated by a similar method, using electrolytes without CH_4N_2S or NH_4Cl.

2.3. Characterizations

The morphology and structure information of the as-prepared samples were analyzed by field-emission scanning electron microscope (FESEM, JEOL JSM-7500 F) and transmission electron microscopy (TEM, FEI Titan G2 60–300), equipped with energy-dispersive X-ray spectroscopy (EDX) detectors. X-ray powder diffraction (XRD) patterns were measured on an X-ray diffractometer (Shimadzu XRD-6100) with Cu Kα radiation ($\lambda = 0.154$ nm). Due to the strong signal of PNF, Ni/Ni_xS_y was deposited on carbon fiber paper (CFP) and scraped off for the XRD test. X-ray photoelectron spectroscopy (XPS) measurements were performed on an ESCALab 250Xi electron spectrometer (Thermo Fisher Scientific) equipped with an Al Kα X-ray source. The contact angle was measured on a contact angle goniometer (Theta Flex, Biolin Scientific, Finland).

2.4. Electrochemical measurement

All electrochemical measurements were carried out by an electrochemical workstation (CHI760E, CH Instruments) in a standard three-electrode system. Typically, the graphite rod and Hg/HgO electrode were used as counter electrode and reference electrode, respectively. All potentials were calibrated to the reversible hydrogen electrode (RHE) *via* Nernst equation: $E_{RHE} = E_{Hg/HgO} + 0.059 \times pH + 0.098$. The linear sweep voltammetry (LSV) tests were performed in 1.0 M KOH at a scan rate of 5 mV s^{-1}. All polarization curves were recorded after an activation process until the electrode reached a stable state. The polarization curves were calibrated with solution resistance by the following equation: $E_{iR \ corrected} = E - iR$. Electrochemical impedance spectroscopy (EIS) was performed at -0.1 V *vs.* RHE with a frequency range from 100 kHz to 0.1 Hz. The chronogeometry test was applied at a constant current density of 100 mA cm^{-2}. Electrochemical active surface area (ECSA) was calculated according to the equation: $ECSA = C_{dl}/C_s$, where C_{dl} was the double-layer capacitance and C_s was the specific capacitance. Cyclic voltammetry (CV) curves with scan rates from 10 to 50 mV s^{-1} were measured to evaluate the C_{dl}, which was obtained by plotting $\Delta j/2$ against the scan rates. Besides, the loading mass of Pt/C and IrO_2 on PNF was 2 mg cm^{-2}.

2.5. Theoretical calculations

Density functional theory calculations were performed using the Vienna Ab-initio Simulation Package (VASP) with the Perdew-Burke-Ernzehof functional of the generalized gradient approximation [45–47]. The Monkhorst-Pack *k*-mesh of $3 \times 2 \times 1$ and plane-wave energy cut-off of 400 eV was used for all structures. NiS (012) and Ni/Ni_xS_y heterostructure were built for adsorption energy calculations with DFT-D2 correction. A 15 Å thick vacuum layer in z direction was employed to eliminate the interaction between the neighboring layers. The computational structures were relaxed until a maximum threshold force was less than 0.05 eV $Å^{-1}$ and the total energy convergence criterion was 10^{-5} eV. All the parameters were optimized in terms of accuracy and computational time using results of preliminary calculations.

3. Results and discussion

3.1. Synthesis and characterizations

A facile two-step electrodeposition process was utilized to fabricate the Ni/Ni_xS_y-PNF electrode, which involves the preparation of PNF

substrate and the following *in-situ* growth of Ni/Ni$_x$S$_y$ heterostructure on the substrate (Fig. 1). First, the PNF substrate was prepared by a dynamic bubble template method in a two-electrode system at room temperature. When an ultrahigh cathodic current density was applied to the commercial NF, Ni^{2+} reduction reaction and HER occurred simultaneously. The porous structure of PNF was fabricated through the generated hydrogen bubbles that work as a dynamic template [48–50]. Compared with pristine NF, the obtained PNF substrate with a multi-level porous structure can provide abundant active sites for catalyst loading and facilitate mass transfer (Fig. 2a and S1). Subsequently, the Ni/Ni$_x$S$_y$ heterostructure is grown on the PNF *via* the simultaneous electrodeposition of Ni and Ni$_x$S$_y$. During the electrodeposition process, some Ni^{2+} are reduced to metallic Ni nanoparticles, while other Ni^{2+} react with S^{2-} produced by thiourea decomposition (x Ni^{2+} + y CH$_4$N$_2$S + 2x e$^-$ → Ni$_x$S$_y$ + y CN$^-$ + y NH$_4^+$) to form Ni$_x$S$_y$ nanosheet arrays [51,52]. As shown in Figs. 2b and 2c, the Ni nanoparticles and Ni$_x$S$_y$ nanosheet arrays are grown on the PNF substrate to form Ni/Ni$_x$S$_y$-PNF electrode. The hierarchical porous structure of Ni/Ni$_x$S$_y$-PNF increases the effective active surface area and especially promotes mass transfer and bubble detachment at high current densities. For comparison, Ni-PNF and NiS-PNF electrodes were also fabricated using the same method. Fig. S2 shows the FESEM images of Ni-PNF and NiS-PNF electrodes. The Ni-PNF electrode has excess Ni nanoparticles on the surface and pores of PNF, which results in channel blockage of PNF. Moreover, the NiS-PNF exhibits a similar nanosheet array structure to that of Ni/Ni$_x$S$_y$-PNF. The TEM image of NiS also shows its nanosheet structure (Fig. S3). Notably, the TEM image of Ni/Ni$_x$S$_y$ heterostructure demonstrates the tightly contacted of Ni nanoparticles and Ni$_x$S$_y$ nanosheets (Fig. 2d). Fig. 2e shows the HRTEM image of Ni/Ni$_x$S$_y$ heterostructure interface, where the Ni nanoparticles are crystalline and the Ni$_x$S$_y$ nanosheet exhibits an amorphous structure. The lattice spacing of 0.203 nm corresponds to the (111) plane of metallic Ni (JCPDS No. 04–0850). The EDS mapping indicates the existence and uniform distribution of Ni and S elements in the Ni/Ni$_x$S$_y$-PNF catalyst (Fig. 2f and S4).

A porous layer composed of nickel nanoparticles on the surface of NF changes its pristine hydrophobic property, endowing PNF with a super-hydrophilic surface (Fig. 3a). The super-hydrophilicity of PNF promotes the contact between electrode surface and electrolyte, which reduces the adhesion of bubbles and facilitated the loading of active electrocatalysts [53]. After *in-situ* growth of Ni/Ni$_x$S$_y$, the Ni/Ni$_x$S$_y$-PNF electrode also exhibits super-hydrophilicity (Fig. S5). XRD analysis was conducted to reveal the crystal structures of NiS and Ni/Ni$_x$S$_y$. To prevent the strong signal of PNF substrate from covering the sign of the supported catalyst, NiS and Ni/Ni$_x$S$_y$ were deposited on carbon fiber paper and scraped off for the XRD testing. As the XRD pattern shown in Fig. 3b, the as-prepared Ni/Ni$_x$S$_y$ shows characteristic peaks located at 44.5° and 51.8°, which corresponds to the (111) and (200) plane of metallic Ni (JCPDS No. 04–0850). For the NiS sample, the peak located at 59.7° corresponded to the (012) plane of NiS (JCPDS No. 12–0041). However, this peak disappears in the Ni/Ni$_x$S$_y$, indicating that the formation of Ni/Ni$_x$S$_y$ heterostructure resulted in the amorphization of NiS. XPS was then conducted to investigate the valence states of elements on the

catalyst surface. In the Ni 2p spectra of NiS-PNF and Ni/Ni$_x$S$_y$-PNF, two peaks located at 855.7 and 873.4 eV are assigned to Ni^{2+}, while the peaks locate at 861.0 and 878.4 eV are two satellite peaks (Fig. 3c) [54]. In addition, the characteristic peak of Ni/Ni$_x$S$_y$-PNF at 852.6 eV corresponds to the metallic Ni [55], which is consistent with the XRD and HRTEM results. Note that the Ni 2p peaks of Ni/Ni$_x$S$_y$-PNF present a negative shift for Ni^{2+}, indicating the strong electronic interactions between Ni and Ni$_x$S$_y$ at the heterostructure interface. Fig. 3d shows the S 2p spectra of NiS-PNF and Ni/Ni$_x$S$_y$-PNF. The two peaks locate at 162.4 and 163.6 eV are assigned to S 2p$_{3/2}$ and S 2p$_{1/2}$, respectively, indicating the existence of the Ni-S bond [21].

3.2. Electrochemical performance

The as-prepared electrodes were directly used as working electrodes to evaluate the electrocatalytic HER performance in 1.0 M KOH using a standard three-electrode system. The graphite rod and the Hg/HgO electrodes (1.0 M KOH) were employed as counter and reference electrodes, respectively. All polarization curves were recorded at a scan rate of 5 mV s^{-1} after activation until a stable state was achieved. To precisely regulate the electronic structure of Ni/Ni$_x$S$_y$ heterostructure interface, we synthesized a series of Ni/Ni$_x$S$_y$-PNF electrodes with different NH$_4$Cl-containing electrolytes, electrodeposition potentials, and reaction times, respectively. The optimized Ni/Ni$_x$S$_y$-PNF electrode with NH$_4$Cl content of 300 mg, electrodeposition potential of − 1.8 V (*vs.* Ag/AgCl), and reaction time of 600 s showed the best electrochemical HER performance (Fig. S6).

For comparison, the HER performance of PNF, Ni-PNF, NiS-PNF, and Pt/C-PNF (commercial Pt/C loaded on PNF) electrodes, were also measured under the same conditions. As the linear sweep voltammetry (LSV) curves shown in Fig. 4a, the overpotential of Ni/Ni$_x$S$_y$-PNF electrode is significantly lower than that of Ni-PNF and NiS-PNF electrodes, indicating enhanced HER activity of Ni/Ni$_x$S$_y$ heterostructure. Notably, the overpotentials at 100 and 500 mA cm^{-2} are 61 and 121 mV, respectively, for the Ni/Ni$_x$S$_y$-PNF electrode, which exceeds those of the benchmark Pt/C-PNF electrode (112 and 216 mV). In addition, the smaller Tafel slope of 83 mV dec^{-1} for the Ni/Ni$_x$S$_y$-PNF electrode demonstrates more favorable reaction kinetics for HER, which is superior to the PNF (92 mV dec^{-1}), Ni-PNF (156 mV dec^{-1}), NiS-PNF (89 mV dec^{-1}), and Pt/C-PNF (138 mV dec^{-1}) electrodes (Fig. 4b). Note that the HER activity of the Ni/Ni$_x$S$_y$-PNF electrode is also better than that of most previously reported alkaline HER catalysts (Table S1). EIS measurement was conducted to evaluate the interfacial charge transfer kinetics. The Nyquist diagram with semicircular features corresponded to an equivalent circuit (EC) composed of electrolyte resistance, charge-transfer resistance (R$_{ct}$), and constant phase element. As displayed in Fig. 4c, the Ni/Ni$_x$S$_y$-PNF electrode possesses the smallest semicircle radius among these electrodes, indicating its rapid charge transfer kinetics. Besides, the Ni/Ni$_x$S$_y$-PNF (11.7 mF cm^{-2}) electrode has a larger C$_{dl}$ than that of Ni-PNF (3.9 mF cm^{-2}) and NiS-PNF (9.0 mF cm^{-2}), suggesting the construction of Ni/Ni$_x$S$_y$ heterostructure facilitates exposure of more active sites (Fig. S7). Furthermore, the ECSA normalized HER polarization curves are measured to evaluate the intrinsic activity, which confirms the enhanced intrinsic HER activity of the Ni/Ni$_x$S$_y$-PNF electrode compared to the Ni-PNF and NiS-PNF electrodes (Fig. S8). The stability of Ni/Ni$_x$S$_y$-PNF electrode is evaluated by chronopotentiometry test at a high current density of 100 mA cm^{-2}. The chronopotentiometry curves reveal that the Ni/Ni$_x$S$_y$-PNF electrode operates stably for 12 h with negligible activity loss (Fig. 4d). Afterward, the structure and composition of the Ni/Ni$_x$S$_y$-PNF were evaluated after the HER stability test. The FESEM image shows that the nanosheet array structure of Ni/Ni$_x$S$_y$ heterostructure is preserved after the HER process (Fig. S9). In addition, the XRD and XPS analysis indicates that the chemical composition and valence state exhibits negligible changes after the long-term HER test (Figs. S10 and S11). These results demonstrate the superior durability of Ni/Ni$_x$S$_y$-PNF for HER.
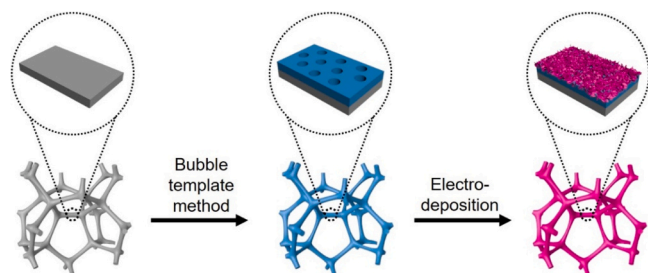

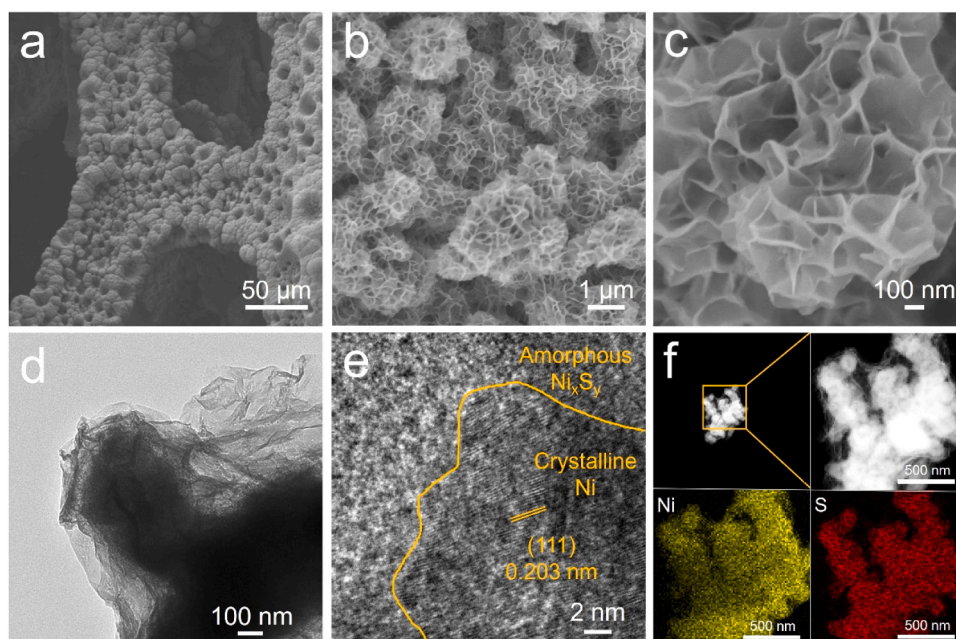**Fig. 1.** Schematic illustration of the synthesis of Ni/Ni$_x$S$_y$-PNF electrode.

Fig. 2. FESEM images of (a) PNF, (b, c) Ni/Ni$_x$S$_y$-PNF. (d) TEM and (e) HRTEM images of Ni/Ni$_x$S$_y$ heterostructure. (f) EDS mapping of Ni/Ni$_x$S$_y$.
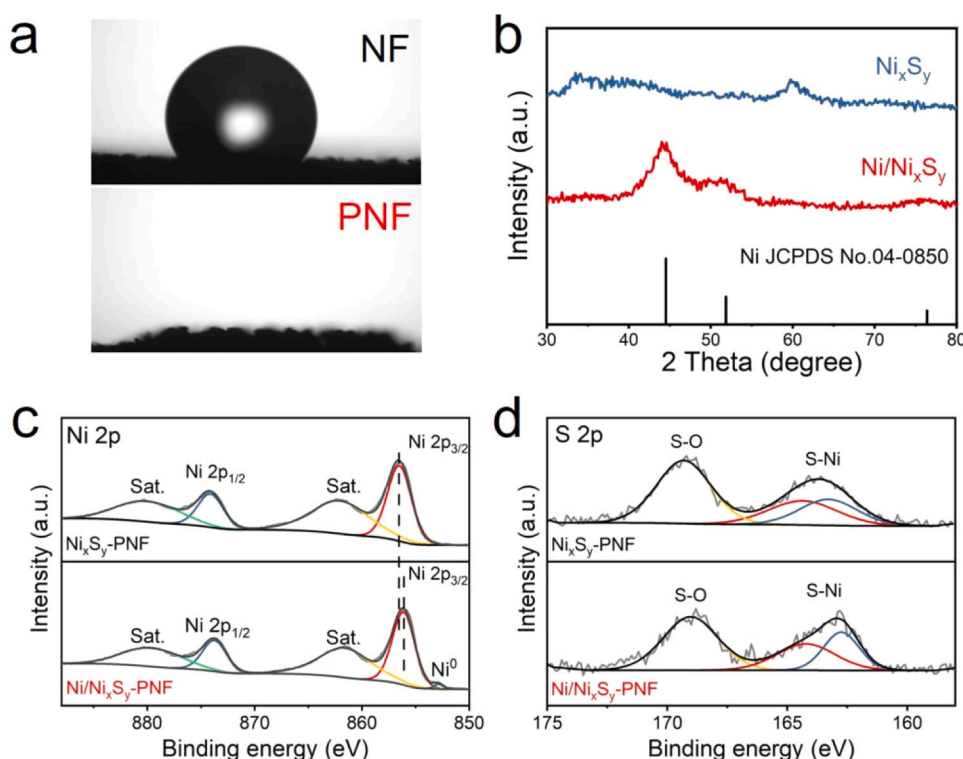

Fig. 3. (a) Contact angles of NF and PNF. (b) XRD patterns of NiS and Ni/Ni$_x$S$_y$. High-resolution (c) Ni 2p and (d) S 2p spectra of Ni$_x$S$_y$-PNF and Ni/Ni$_x$S$_y$-PNF.

3.3. HER mechanism

Operando EIS tests can identify the rate-determining step and the mechanism of HER in an alkaline medium due to the different frequency dependence of different elementary steps, including the water dissociation process (Volmer step, $H_2O + e^- \rightarrow H* + OH^-$) and proton reduction process (Heyrovsky step, $H_2O + H* + e^- \rightarrow H_2 + OH^-$ or Tafel step, $2\,H* \rightarrow H_2$) [56–58]. The EC for HER is shown in Fig. 5a, which typically consisted of the electrolyte resistance, the interfacial reaction

charge transfer process, the reaction intermediate accumulation process, and the electron transfer from the cathode to the reaction interface [56]. The operando EIS tests were tested at different overpotentials of 0, 50, 100, 150, 200, 250, and 300 mV. The operando Bode plots of NiS-PNF and Ni/Ni$_x$S$_y$-PNF electrodes are shown in Fig. 5b, 5c, and S12. The high-frequency region corresponds to the electron transfer from the inside of catalysts to the active sites on the surface, while the low-frequency region related to the Volmer step, respectively [58,59]. The negligible change in phase angle in the high-frequency region for
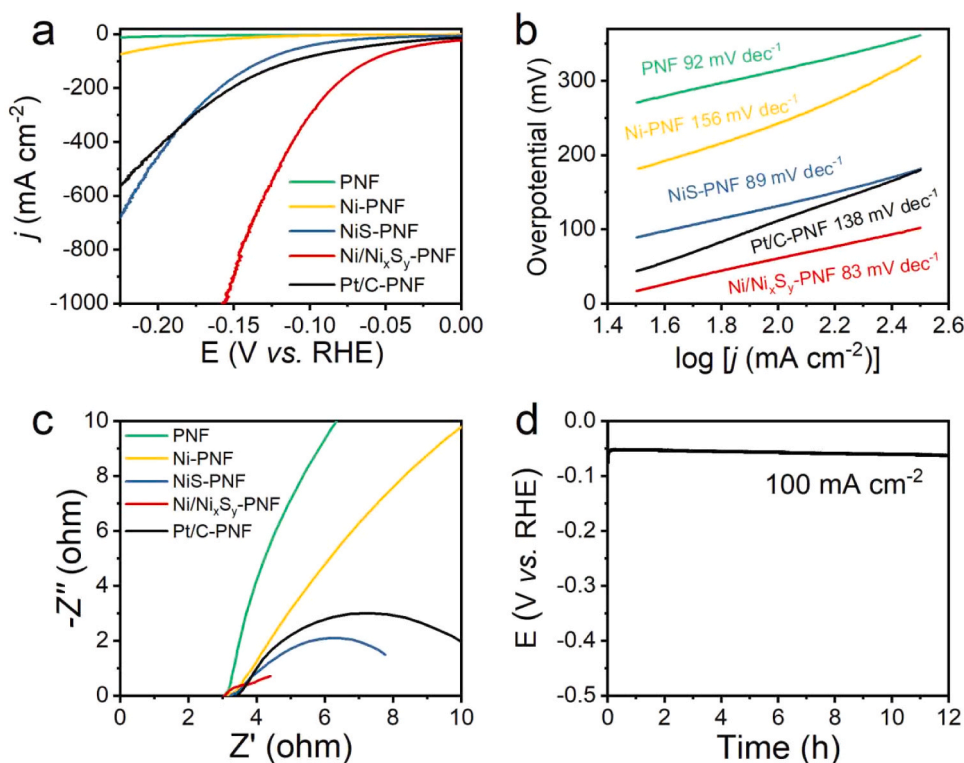
Fig. 4. Electrochemical HER performance. (a) HER polarization curves, (b) Tafel plots, and (c) Nyquist plots of PNF, Ni-PNF, NiS-PNF, Ni/NixSy-PNF, and Pt/C-PNF electrodes. (d) Chronopotentiometry curves of Ni/NixSy-PNF electrode.
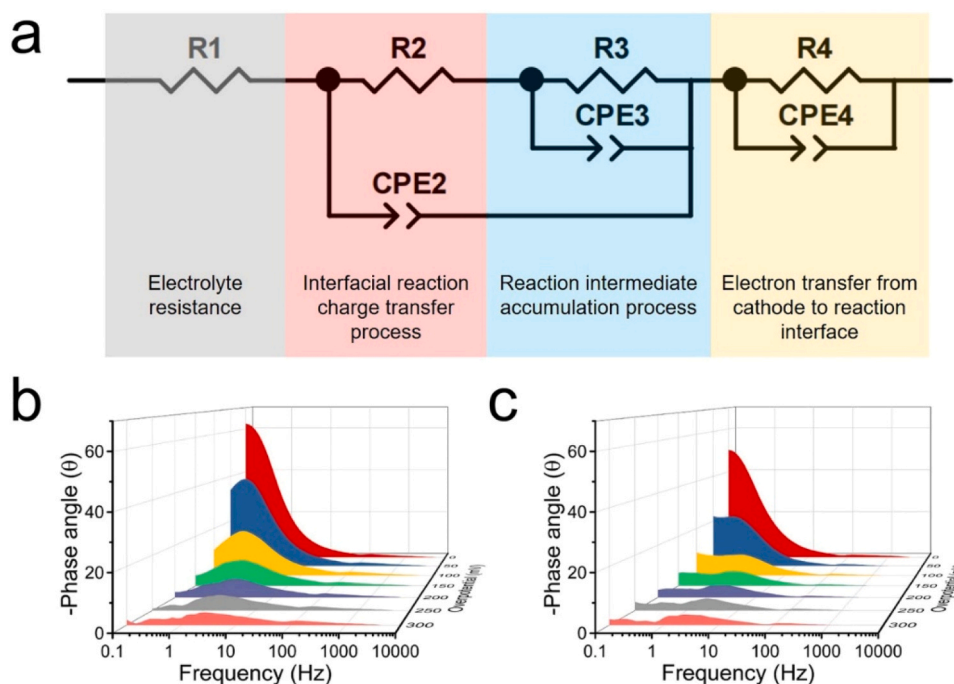

Fig. 5. (a) The EC of HER. Operando Bode plots of (b) NiS-PNF and (c) Ni/NixSy-PNF electrodes.

both electrodes indicates that the electron transfer process in the electrode from internal to the surface active sites is similar. In particular, Ni/NixSy-PNF electrode shows a significantly faster decrease of phase angle in the low-frequency region, suggesting that the Ni/NixSy-PNF electrode has a faster Volmer step than the NiS-PNF electrode during the HER in alkaline media. These results demonstrate that the Ni/NixSy

heterostructure promotes the water dissociation process, leading to the enhanced HER activity of Ni/NixSy-PNF.

Density functional theory (DFT) calculations were further performed to investigate the alkaline HER behaviors of NiS and Ni/NixSy (Figs. S13 and S14). From the energetic perspective, the Ni/NixSy heterostructure displays much stronger H_2O adsorption ability (-1.92 eV) than that of

NiS (−0.27 eV) (Fig. S15). The favorable adsorption of H_2O improves the efficiency of subsequent water dissociation process [60,61].

3.4. Alkaline water electrolysis performance

The above results indicated that the Ni/Ni_xS_y-PNF electrode had superior HER activity and excellent stability. Thus, we evaluated its applicability for overall water splitting. We used the Ni/Ni_xS_y-PNF electrode as the cathode and a Fe-Ni_3S_2-PNF electrode as the anode to measure the overall water splitting performance in 1.0 M KOH at room temperature. The Fe-Ni_3S_2-PNF electrode was fabricated according to our previous work [51]. As demonstrated in Fig. 6a, the Ni/Ni_xS_y-PNF|| Fe-Ni_3S_2-PNF electrolyser only needs low voltages of 1.32 and 1.69 V to reach 10 and 100 mA cm^{-2}, respectively. The activity of the Ni/Ni_x-S_y-PNF||Fe-Ni_3S_2-PNF electrolyser for overall water splitting outperforms the benchmark Pt/C-PNF||IrO_2-PNF electrolyser and many previously reported works (Table S2). The chronopotentiometry curves in Fig. 6b demonstrate that the Ni/Ni_xS_y-PNF||Fe-Ni_3S_2-PNF electrolyser can operate stably at 100 mA cm^{-2} for 12 h, while the Pt/C-PNF|| IrO_2-PNF electrolyser shows rapid decay under the same conditions. Inspired by the impressive overall water splitting activity and stability of the Ni/Ni_xS_y-PNF||Fe-Ni_3S_2-PNF electrolyser, we further operated it under industrial conditions (30 wt% KOH, 85 °C) to evaluate the possibility for practical applications. The Ni/Ni_xS_y-PNF||Fe-Ni_3S_2-PNF electrolyser exhibits a much lower voltage of 1.72 V to achieve a current density of 500 mA cm^{-2} than that of the commercial RN= |RN electrolyser (2.01 V) (Fig. 6c). As shown in Fig. 6d, the Ni/Ni_xS_y-PNF|| Fe-Ni_3S_2-PNF electrolyser displays excellent stability with negligible voltage increase at 500 mA cm^{-2} for 120 h, while the performance of commercial RN= |RN electrolyser shows a rapid decay. The impressive activity and durability of Ni/Ni_xS_y-PNF||Fe-Ni_3S_2-PNF electrolyser is attributed to the following factors: (1) PNF substrate with super-hydrophilic surface increases loading of catalyst and facilitates the intimate contact between catalyst and substrate; (2) The unique electronic structure of Ni/Ni_xS_y heterostructure and Fe-Ni_3S_2, which has optimized adsorbing strength of intermediates for HER and OER, respectively. (3) The hierarchical porous structure of the electrode facilitates the mass transfer and bubble detachment process at high-current-density conditions. These results demonstrate the promising potential of the Ni/Ni_xS_y-PNF electrode for practical alkaline water electrolysis (Fig. 6d).

4. Conclusions

In summary, we developed a hierarchical porous Ni/Ni_xS_y-PNF electrode with superior HER activity and excellent durability. The Ni/ Ni_xS_y-PNF electrode with super-hydrophilic surface and hierarchical porous structure efficiently promotes mass transfer and bubble release process at high current densities. In addition, the electron transfer between Ni and Ni_xS_y optimizes the electron structure of the crystalline/ amorphous Ni/Ni_xS_y heterostructure interface, leading to the enhanced HER activity. Consequently, the Ni/Ni_xS_y-PNF electrode features a low overpotential of 61 mV at 100 mA cm^{-2} and a small Tafel slope of 83 mV dec^{-1} in 1.0 M KOH. Operando EIS tests demonstrate that the highly active Ni/Ni_xS_y heterostructure interface facilitates the reaction kinetic of water dissociation step during the HER process. DFT calculations reveals that the enhanced HER activity of Ni/Ni_xS_y heterostructure is attributed to the stronger H_2O adsorption. The Ni/Ni_xS_y-PNF||Fe-Ni_3S_2-PNF electrolyser exhibits extremely low voltage at 1.32 V to achieve 10 mA cm^{-2} for two-electrode overall water splitting. Impressively, the alkaline water electrolysis performance under industrial conditions of Ni/Ni_xS_y-PNF||Fe-Ni_3S_2-PNF electrolyser exceeds the commercial RN electrode. This facile method provides a promising approach to the fabrication of advanced alkaline water electrolysis electrodes.
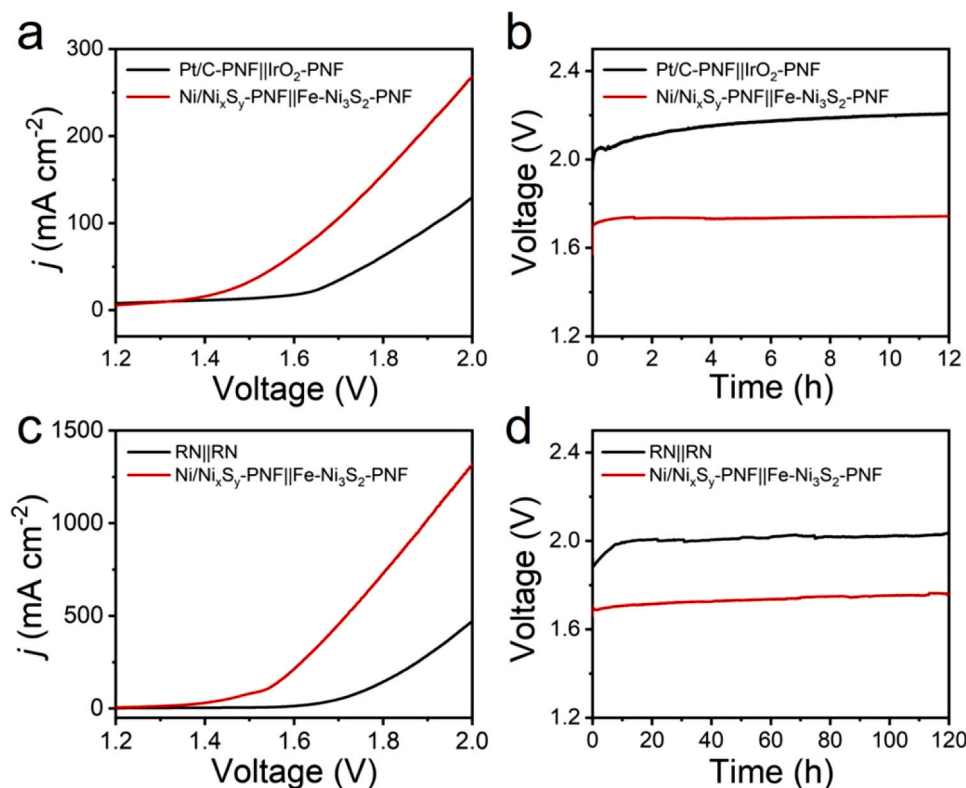

Fig. 6. (a) Polarization curves and (b) chronopotentiometry curves of the Pt/C-PNF||IrO_2-PNF and Ni/Ni_xS_y-PNF||Fe-Ni_3S_2-PNF electrolyser for overall water splitting in 1.0 M KOH. (c) Polarization curves and (d) chronopotentiometry curves of the commercial Raney nickel (RN)||RN and Ni/Ni_xS_y-PNF||Fe-Ni_3S_2-PNF electrolyser for alkaline water electrolysis under industrial conditions (30 wt% KOH, 85 °C).

CRediT authorship contribution statement

Bo Zhong: Conceptualization, Investigation, Methodology, Writing – original draft. **Sijie Wan:** Software, Investigation. **Panyong Kuang:** Investigation. **Bei Cheng:** Resources. **Luo Yu:** Formal analysis, Resources, Methodology, Writing – review & editing. **Jiaguo Yu:** Funding acquisition, Resources, Methodology, Writing – review & editing.

Declaration of Competing Interest

The authors declare that they have no known competing financial interests or personal relationships that could have appeared to influence the work reported in this paper.

Data Availability

Data will be made available on request.

Acknowledgments

Appendix A. Supporting information

Supplementary data associated with this article can be found in the online version at doi:10.1016/j.apcatb.2023.123195.

References

[1] P. Kuang, Y. Wang, B. Zhu, F. Xia, C.-W. Tung, J. Wu, H.M. Chen, J. Yu, Pt single atoms supported on N-Doped mesoporous hollow carbon spheres with enhanced electrocatalytic H_2-evolution activity, Adv. Mater. 33 (2021) 2008599.

[2] Y. Ren, S. Zhu, Y. Liang, Z. Li, S. Wu, C. Chang, S. Luo, Z. Cui, Hierarchical $Ni_3S_4@MoS_2$ nanocomposites as efficient electrocatalysts for hydrogen evolution reaction, J. Mater. Sci. Technol. 95 (2021) 70–77.

[3] R. Li, P. Kuang, S. Wageh, A.A. Al-Ghamdi, H. Tang, J. Yu, Potential-dependent reconstruction of Ni-based cuboid arrays for highly efficient hydrogen evolution coupled with electro-oxidation of organic compound, Chem. Eng. J. 453 (2023), 139797.

[4] Z. Ni, C. Luo, B. Cheng, P. Kuang, Y. Li, J. Yu, Construction of hierarchical and self-supported NiFe-Pt$_3$Ir electrode for hydrogen production with industrial current density, Appl. Catal. B-Environ. 321 (2023) 122072.

[5] C. Huang, J. Zhou, D. Duan, Q. Zhou, J. Wang, B. Peng, L. Yu, Y. Yu, Roles of heteroatoms in electrocatalysts for alkaline water splitting: a review focusing on the reaction mechanism, Chin. J. Catal. 43 (2022) 2091–2110.

[6] Y. Wang, X. Huang, Z. Wei, Recent developments in the use of single-atom catalysts for water splitting, Chin. J. Catal. 42 (2021) 1269–1286.

[7] T. Cui, X. Zhai, L. Guo, J.-Q. Chi, Y. Zhang, J. Zhu, X. Sun, L. Wang, Controllable synthesis of a self-assembled ultralow Ru, Ni-doped Fe_2O_3 lily as a bifunctional electrocatalyst for large-current-density alkaline seawater electrolysis, Chin. J. Catal. 43 (2022) 2202–2211.

[8] P. Kuang, M. Sayed, J. Fan, B. Cheng, J. Yu, 3D graphene-based H_2-production photocatalyst and electrocatalyst, Adv. Energy Mater. 10 (2020) 1903802.

[9] K. Sun, Y.Q. Zhao, J. Yin, J. Jin, H.W. Liu, P.X. Xi, Surface modification of $NiCo_2O_4$ nanowires using organic ligands for overall water splitting, Acta Phys. -Chim. Sin. 38 (2022) 2107005.

[10] L. Lv, L.Y. Zhang, X.B. He, H. Yuan, S.X. Ouyang, T.R. Zhang, Energy-efficient hydrogen production via electrochemical methanol oxidation using a bifunctional nickel nanoparticle-embedded carbon prism-like microrod electrode, Acta Phys. -Chim. Sin. 37 (2021) 2007079.

[11] C. Huang, L. Yu, W. Zhang, Q. Xiao, J. Zhou, Y. Zhang, P. An, J. Zhang, Y. Yu, N-doped Ni-Mo based sulfides for high-efficiency and stable hydrogen evolution reaction, Appl. Catal. B-Environ. 276 (2020) 119137.

[12] L. Liao, C. Cheng, H. Zhou, Y. Qi, D. Li, F. Cai, B. Yu, R. Long, F. Yu, Accelerating pH-universal hydrogen-evolving activity of a hierarchical hybrid of cobalt and dinickel phosphides by interfacial chemical bonds, Mater. Today Phys. 22 (2022), 100589.

[13] W. Yu, M.H. Richter, P. Buabthong, I.A. Moreno-Hernandez, C.G. Read, E. Simonoff, B.S. Brunschwig, N.S. Lewis, Investigations of the stability of etched or platinized p-InP(100) photocathodes for solar-driven hydrogen evolution in acidic or alkaline aqueous electrolytes, Energy Environ. Sci. 14 (2021) 6007–6020.

[14] R. Li, P. Kuang, L. Wang, H. Tang, J. Yu, Engineering 2D NiO/Ni_3S_2 heterointerface electrocatalyst for highly efficient hydrogen production coupled with benzyl alcohol oxidation, Chem. Eng. J. 431 (2022), 134137.

[15] W. Zhao, C. Luo, Y. Lin, G.-B. Wang, H.M. Chen, P. Kuang, J. Yu, Pt–Ru dimer electrocatalyst with electron redistribution for hydrogen evolution reaction, ACS Catal. 12 (2022) 5540–5548.

[16] M. Gong, W. Zhou, M.-C. Tsai, J. Zhou, M. Guan, M.-C. Lin, B. Zhang, Y. Hu, D.-Y. Wang, J. Yang, S.J. Pennycook, B.-J. Hwang, H. Dai, Nanoscale nickel oxide/nickel heterostructures for active hydrogen evolution electrocatalysis, Nat. Commun. 5 (2014) 4695.

[17] K. Lu, Y. Liu, F. Lin, I.A. Cordova, S. Gao, B. Li, B. Peng, H. Xu, J. Kaelin, D. Coliz, C. Wang, Y. Shao, Y. Cheng, Li_xNiO/Ni heterostructure with strong basic lattice oxygen enables electrocatalytic hydrogen evolution with Pt-like activity, J. Am. Chem. Soc. 142 (2020) 12613–12619.

[18] Z.-H. Xue, H. Su, Q.-Y. Yu, B. Zhang, H.-H. Wang, X.-H. Li, J.-S. Chen, Janus Co/CoP nanoparticles as efficient Mott–Schottky electrocatalysts for overall water splitting in wide pH range, Adv. Energy Mater. 7 (2017) 1602355.

[19] Z. Guo, G. Tian, L. Liu, B. Zhang, Q. Wu, Y. Cao, J. Tu, L. Ding, X. Zhang, Phosphorus substitution into Co_3S_4 nanoneedle arrays for efficient hydrogen evolution catalysis, J. Mater. Sci. Technol. 89 (2021) 52–58.

[20] Y. Wang, B. Zhu, B. Cheng, W. Macyk, P. Kuang, J. Yu, Hollow carbon sphere-supported Pt/CoO_x hybrid with excellent hydrogen evolution activity and stability in acidic environment, Appl. Catal. B-Environ. 314 (2022), 121503.

[21] Y. Wu, X. Liu, D. Han, X. Song, L. Shi, Y. Song, S. Niu, Y. Xie, J. Cai, S. Wu, J. Kang, J. Zhou, Z. Chen, X. Zheng, X. Xiao, G. Wang, Electron density modulation of $NiCo_2S_4$ nanowires by nitrogen incorporation for highly efficient hydrogen evolution catalysis, Nat. Commun. 9 (2018) 1425.

[22] B. Zhong, L. Zhang, J. Yu, K. Fan, Ultrafine iron-cobalt nanoparticles embedded in nitrogen-doped porous carbon matrix for oxygen reduction reaction and zinc-air batteries, J. Colloid Interface Sci. 546 (2019) 113–121.

[23] D. Cao, B. Sheng, Z. Qi, W. Xu, S. Chen, O.A. Moses, R. Long, Y. Xiong, X. Wu, L. Song, Self-optimizing iron phosphorus oxide for stable hydrogen evolution at high current, Appl. Catal. B-Environ. 298 (2021), 120559.

[24] Y. Luo, L. Tang, U. Khan, Q. Yu, H.-M. Cheng, X. Zou, B. Liu, Morphology and surface chemistry engineering toward pH-universal catalysts for hydrogen evolution at high current density, Nat. Commun. 10 (2019) 269.

[25] L. Zhang, J. Zhang, J. Fang, X.-Y. Wang, L. Yin, W. Zhu, Z. Zhuang, Cr-doped CoP nanorod arrays as high-performance hydrogen evolution reaction catalysts at high current density, Small 17 (2021) 2100832.

[26] L. Zhao, Y. Zhang, Z. Zhao, Q.-H. Zhang, L.-B. Huang, L. Gu, G. Lu, J.-S. Hu, L.-J. Wan, Steering elementary steps towards efficient alkaline hydrogen evolution via size-dependent Ni/NiO nanoscale heterosurfaces, Natl. Sci. Rev. 7 (2020) 27–36.

[27] X. Wang, Y. Zheng, W. Sheng, Z.J. Xu, M. Jaroniec, S.-Z. Qiao, Strategies for design of electrocatalysts for hydrogen evolution under alkaline conditions, Mater. Today 36 (2020) 125–138.

[28] S. Schumacher, S. Baha, A. Savan, C. Andronescu, A. Ludwig, High-throughput discovery of hydrogen evolution electrocatalysts in the complex solid solution system Co–Cr–Fe–Mo–Ni, J. Mater. Chem. A 10 (2022) 9981–9987.

[29] M.T. Li, X.Q. Zheng, L. Li, Z.D. Wei, Research progress of hydrogen oxidation and hydrogen evolution reaction mechanism in alkaline media, Acta Phys. -Chim. Sin. 37 (2021) 2007054.

[30] P. Zhai, Y. Zhang, Y. Wu, J. Gao, B. Zhang, S. Cao, Y. Zhang, Z. Li, L. Sun, J. Hou, Engineering active sites on hierarchical transition bimetal oxides/sulfides heterostructure array enabling robust overall water splitting, Nat. Commun. 11 (2020) 5462.

[31] J. Wei, M. Zhou, A. Long, Y. Xue, H. Liao, C. Wei, Z.J. Xu, Heterostructured electrocatalysts for hydrogen evolution reaction under alkaline conditions, Nano-Micro Lett. 10 (2018) 75.

[32] Q. Luo, L. Sun, Y. Zhao, C. Wang, H. Xin, D. Li, F. Ma, Synergistic effects of 1T MoS_2 and interface engineering on hollow NiCoP nanorods for enhanced hydrogen evolution activity, J. Mater. Sci. Technol. 145 (2023) 165–173.

[33] A. Mondal, A. Vomiero, 2D transition metal dichalcogenides-based electrocatalysts for hydrogen evolution reaction, Adv. Funct. Mater. 32 (2022) 2208994.

[34] P. Wang, X. Zhang, J. Zhang, S. Wan, S. Guo, G. Lu, J. Yao, X. Huang, Precise tuning in platinum-nickel/nickel sulfide interface nanowires for synergistic hydrogen evolution catalysis, Nat. Commun. 8 (2017) 14580.

[35] H. Wang, W. Zhang, X. Zhang, S. Hu, Z. Zhang, W. Zhou, H. Liu, Multi-interface collaboration of graphene cross-linked $NiS-NiS_2-Ni_3S_4$ polymorph foam towards robust hydrogen evolution in alkaline electrolyte, Nano Res. 14 (2021) 4857–4864.

[36] L. Wang, J. Cao, C. Lei, Q. Dai, B. Yang, Z. Li, X. Zhang, C. Yuan, L. Lei, Y. Hou, Strongly coupled 3D N-doped MoO_2/Ni_3S_2 hybrid for high current density hydrogen evolution electrocatalysis and biomass upgrading, ACS Appl. Mater. Interfaces 11 (2019) 27743–27750.

[37] Z. Sun, X. Wang, M. Yuan, H. Yang, Y. Su, K. Shi, C. Nan, H. Li, G. Sun, J. Zhu, X. Yang, S. Chen, "Lewis Base-Hungry" amorphous–crystalline nickel borate–nickel sulfide heterostructures by in situ structural engineering as effective bifunctional electrocatalysts toward overall water splitting, ACS Appl. Mater. Interfaces 12 (2020) 23896–23903.

[38] H. Liu, X. Xie, Y. Luo, Z. Cui, Q. Yu, Z. Gao, Z. Zhang, F. Yang, X. Kang, S. Ge, S. Li, X. Gao, G. Chai, L. Liu, B. Liu, Dual interfacial engineering of a Chevrel phase electrode material for stable hydrogen evolution at 2500 mA cm^{-2}, Nat. Commun. 13 (2022) 6382.

[39] L. Wan, M. Pang, J. Le, Z. Xu, H. Zhou, Q. Xu, B. Wang, Oriented intergrowth of the catalyst layer in membrane electrode assembly for alkaline water electrolysis, Nat. Commun. 13 (2022) 7956.

[40] C. Li, J. Hou, Z. Wu, K. Guo, D. Wang, T. Zhai, H. Li, Acid promoted Ni/NiO monolithic electrode for overall water splitting in alkaline medium, Sci. China Mater. 60 (2017) 918–928.

[41] H. Sun, Z. Yan, F. Liu, W. Xu, F. Cheng, J. Chen, Self-supported transition-metal-based electrocatalysts for hydrogen and oxygen evolution, Adv. Mater. 32 (2020) 1806326.

[42] P. Liu, B. Chen, C. Liang, W. Yao, Y. Cui, S. Hu, P. Zou, H. Zhang, H.J. Fan, C. Yang, Tip-enhanced electric field: a new mechanism promoting mass transfer in oxygen evolution reactions, Adv. Mater. 33 (2021) 2007377.

[43] Y. Zhou, N. Jin, Y. Ma, Y. Cui, L. Wang, Y. Kwon, W.-K. Lee, W. Zhang, H. Ge, J. Zhang, Tube-sponge-inspired hierarchical electrocatalysts with boosted mass and electron transfer for efficient oxygen evolution, Adv. Mater. (2022) 2209500.

[44] X. Xiao, X. Wang, X. Jiang, S. Song, D. Huang, L. Yu, Y. Zhang, S. Chen, M. Wang, Y. Shen, Z. Ren, In situ growth of Ru nanoparticles on (Fe,Ni)(OH)$_2$ to boost hydrogen evolution activity at high current density in alkaline media, Small Methods 4 (2020) 1900796.

[45] G. Kresse, J. Hafner, Ab initio molecular dynamics for liquid metals, Phys. Rev. B 47 (1993) 558–561.

[46] J.P. Perdew, K. Burke, M. Ernzerhof, Generalized gradient approximation made simple, Phys. Rev. Lett. 77 (1996) 3865–3868.

[47] B. Hammer, L.B. Hansen, J.K. Nørskov, Improved adsorption energetics within density-functional theory using revised Perdew-Burke-Ernzerhof functionals, Phys. Rev. B 59 (1999) 7413–7421.

[48] B. Zhong, P. Kuang, L. Wang, J. Yu, Hierarchical porous nickel supported NiFeO$_x$H$_y$ nanosheets for efficient and robust oxygen evolution electrocatalyst under industrial condition, Appl. Catal. B-Environ. 299 (2021), 120668.

[49] B. You, X. Liu, G. Hu, S. Gul, J. Yano, D.-E. Jiang, Y. Sun, Universal surface engineering of transition metals for superior electrocatalytic hydrogen evolution in neutral water, J. Am. Chem. Soc. 139 (2017) 12283–12290.

[50] F. Song, W. Li, J. Yang, G. Han, P. Liao, Y. Sun, Interfacing nickel nitride and nickel boosts both electrocatalytic hydrogen evolution and oxidation reactions, Nat. Commun. 9 (2018) 4531.

[51] B. Zhong, B. Cheng, Y. Zhu, R. Ding, P. Kuang, J. Yu, Hierarchically porous nickel foam supported Fe-Ni$_3$S$_2$ electrode for high-current–density alkaline water splitting, J. Colloid Interface Sci. 629 (2023) 846–853.

[52] J. Xu, Y. Sun, M. Lu, L. Wang, J. Zhang, X. Liu, One-step electrodeposition fabrication of Ni$_3$S$_2$ nanosheet arrays on Ni foam as an advanced electrode for asymmetric supercapacitors, Sci. China Mater. 62 (2019) 699–710.

[53] H. Li, S. Chen, Y. Zhang, Q. Zhang, X. Jia, Q. Zhang, L. Gu, X. Sun, L. Song, X. Wang, Systematic design of superaerophobic nanotube-array electrode comprised of transition-metal sulfides for overall water splitting, Nat. Commun. 9 (2018) 2452.

[54] S. Lyu, C. Guo, J. Wang, Z. Li, B. Yang, L. Lei, L. Wang, J. Xiao, T. Zhang, Y. Hou, Exceptional catalytic activity of oxygen evolution reaction via two-dimensional graphene multilayer confined metal-organic frameworks, Nat. Commun. 13 (2022) 6171.

[55] Q. Hu, Z. Chen, J. Wang, X. Zheng, X. Han, Y. Deng, W. Hu, Nanoporous nickel with rich adsorbed oxygen for efficient alkaline hydrogen evolution electrocatalysis, Sci. China Mater. 65 (2022) 1825–1832.

[56] W. Chen, B. Wu, Y. Wang, W. Zhou, Y. Li, T. Liu, C. Xie, L. Xu, S. Du, M. Song, D. Wang, Y. liu, Y. Li, J. Liu, Y. Zou, R. Chen, C. Chen, J. Zheng, Y. Li, J. Chen, S. Wang, Deciphering the alternating synergy between interlayer Pt single-atom and NiFe layered double hydroxide for overall water splitting, Energy Environ. Sci. 14 (2021) 6428–6440.

[57] M. Zhang, K. Zhang, X. Ai, X. Liang, Q. Zhang, H. Chen, X. Zou, Theory-guided electrocatalyst engineering: From mechanism analysis to structural design, Chin. J. Catal. 43 (2022) 2987–3018.

[58] K. Dastafkan, X. Shen, R.K. Hocking, Q. Meyer, C. Zhao, Monometallic interphasic synergy via nano-hetero-interfacing for hydrogen evolution in alkaline electrolytes, Nat. Commun. 14 (2023) 547.

[59] V.M. Nikolic, S.L. Maslovara, G.S. Tasic, T.P. Brdaric, P.Z. Lausevic, B.B. Radak, M. P. Marceta, Kaninski, Kinetics of hydrogen evolution reaction in alkaline electrolysis on a Ni cathode in the presence of Ni–Co–Mo based ionic activators, Appl. Catal. B-Environ. 179 (2015) 88–94.

[60] K. Wang, J. Zhou, M. Sun, F. Lin, B. Huang, F. Lv, L. Zeng, Q. Zhang, L. Gu, M. Luo, S. Guo, Cu-doped heterointerfaced Ru/RuSe$_2$ nanosheets with optimized H and H$_2$O adsorption boost hydrogen evolution catalysis, Adv. Mater. 35 (2023) 2300980.

[61] N. Yao, Z. Fan, Z. Xia, F. Wu, P. Zhao, G. Cheng, W. Luo, Constructing the CoO/Co$_4$N heterostructure with an optimized electronic structure to boost alkaline hydrogen evolution electrocatalysis, J. Mater. Chem. A 9 (2021) 18208–18212.